Macía, E.; García-Junceda, A.; Serrano, M.; Hernández-Mayoral, M.; Díaz, L.A.; Campos, M. (2019). Effect of the heating rate on the microstructure of a ferritic ODS steel with four oxide formers (Y-Ti-Al-Zr) consolidated by spark plasma sintering (SPS). *Journal of Nuclear Materials*, v. 518, pp.: 190-201.

DOI: https://doi.org/10.1016/j.jnucmat.2019.02.043

Journal of Nuclear Materials xxx (xxxx) xxx-xxx

Contents lists available at ScienceDirect

Journal of Nuclear Materials

journal homepage: www.elsevier.com

Effect of the heating rate on the microstructure of a ferritic ODS steel with four oxide formers (Y-Ti-Al-Zr) consolidated by spark plasma sintering (SPS)

E. Macía [a, *], A. García-Junceda [b], M. Serrano [c], M. Hernández-Mayoral [c], L.A. Diaz [d], M. Campos [a]

[a] Dept. Materials Science and Engineering, IAAB, Universidad Carlos III de Madrid (UC3M), Av. de la Universidad 30, 28911, Leganés, Spain
[b] IMDEA Materials Institute, C/ Eric Kandel 2, 28906, Getafe, Spain
[c] Structural Materials Division, Technology Department, CIEMAT, Avda de la Complutense 22, 28040, Madrid, Spain
[d] Centro de Investigación en Nanomateriales Y Nanotecnologia(CINN-CSIC-UNIOVI-PA), Grupo de Materiales Nanocompuetos y Bioinspirados, Av. de la Vega, 4-6, 33940, El Entrego, Spain

ARTICLE INFO

Article history:
Received 5 November 2018
Received in revised form 25 January 2019
Accepted 25 February 2019
Available online xxx

Keywords:
ODS steel
Mechanical alloying
Spark plasma sintering (SPS)
EBSD
Yield strength model
Microtensile test
Small punch test (SP)

ABSTRACT

The proposed ODS ferritic steel alloyed with (Y-Ti-Zr-Al) was produced by mechanical alloying (MA) and spark plasma sintering (SPS) to obtain a complex nanostructure. To densify the material, a sintering cycle by SPS was performed at 1100 °C using fast heating rates (from 100 to 600 °C/min). During the attrition of MA powders, the uneven distribution of deformation level and of alloying elements has produced an inhomogeneous recrystallization during the consolidation step. Influence of processing condition was studied by modifying the heating rate of SPS to promote a heterogeneous material with bimodal grain size distribution. The final microstructures were characterized by X-ray diffraction and electron microscopy (SEM and TEM). The mechanical behaviour at R.T. was characterized by means of the Vickers microhardness and micro tensile tests. The good balance obtained between ductility (~22–26%) and yield stress (800–910 MPa) at room temperature is provided by the bimodal grain size distribution. To predict the experimental values depending on the processing conditions, a yield strength model is presented. This model covers the contribution of different strengthening mechanism from solid solution, grain size, dislocation density and oxides precipitation. The model indicates the dislocation density as the major strengthening contribution. In addition, small punch (SP) tests were performed to analyse the response of the material at high temperatures where remarkable properties have been achieved.

1. Introduction

One of the most valuable structural material candidates for severe service conditions are the ODS ferritic steels, especially for nuclear energy applications and particularly for components exposed to higher operation temperatures. Their mechanical properties result from the combination of the high density of nano-oxides dispersed into the ferritic matrix, whose pinning effect and high stability at high temperature increase the creep behaviour, and from the effect of the dual grain size distribution.

The composition of ODS ferritic steels is one of the key issues needed to obtain high performance materials. In this work, Cr and Al are selected to fulfil the corrosion requirements, while W is necessary to maintain these properties at high temperatures through solid solution strengthening. To develop stable nano-oxides with a variable stoichiometry dispersed into the ferritic matrix, Y_2O_3, Ti, and Zr are included in the composition. These nanoprecipitates are used to block the movement of dislocations, improving the mechanical behaviour at high temperatures [1,2]. Traditionally, Y_2O_3 was the main ingredient used to produce nano-oxides [3]. Previous works [4,5] observed that the addition of Ti provided a particle size refinement, developing non-stoichiometric Y-Ti-O nanoclusters whose nature and size increased the performance of the ODS alloys. The bonding energy of Zr-Y-O can be assumed to be far superior to that of Y-Al -O when those compounds are formed in an Fe matrix. That means that initially, Y-Zr-O should form more easily and be more stable than Y-Al-O or Y-Ti-O [6]. Moreover, the presence of Zr could lead to a refinement of the nano-oxides when Al is present, which leads to an increase in the high temperature behaviour, while the corrosion resistance is not modified [7–12]. Further, Zr addition into ferritic ODS steels alloyed with high Al content increases the irradiation damage resistance [13–15] because the newly promoted oxides have superior thermal stability and irradiation tolerance [7]. Moreover, Zr has a small thermal neutron capture cross-section. To understand the effect Zr on the processed microstructure, the materials obtained were compared to others ODS alloys produced in previous works, where the prealloyed powder was consolidated without oxide formers to be used as a reference, or was MA with 0.4 Ti and 0.25 Y_2O_3 wt.% (14Al-ODS-Ti). Both samples were consolidated by SPS using a heating rate of 100 °C/min [16].

On the other side, ODS steels are traditionally obtained by hot isostatic pressing (HIP) or hot extrusion (HE) [17,18]. As an alternative

* Corresponding author.
Email addresses: eric.macia@uc3m.es (E. Macía); andrea.garcia.junceda@imdea.org (A. García-Junceda); marta.serrano@ciemat.es (M. Serrano); m.mayoral@ciemat.es (M. Hernández-Mayoral); la.diaz@cinn.es (L.A. Diaz); monica.campos@uc3m.es (M. Campos)

https://doi.org/10.1016/j.jnucmat.2019.02.043
0022-3115/

Table 1
Composition, in wt.%, and theoretical densities, ρ_{min} and ρ_{max} (g/cm^3)[i], of the processed ferritic ODS alloys (powder label: P: Prealloyed, E: Elemental).

Tag	Prealloyed Fe-14Cr-5Al-3W	Ti	Zr	Y_2O_3	ρ_{min}	ρ_{max}
14ZrODS	Balance[P]	0.4[E]	0.6[E]	0.25[E]	7.21	7.85

i The theoretical density of the ODS is calculated by two approximations: the mixing rule (1) and the density of a compact free of porous (2).$\rho_{max} = \sum w_i \cdot \rho_i$ (1) $\rho_{min} = 1/\Sigma(wi/\rho i)$ (2).

Table 2
SPS cycles modifying the heating rate.

Cycle		Sample Label
1100 °C, 80 MPa, 5 min	100 °C/min	Zr100
	200 °C/min	Zr200
	400 °C/min	Zr400
	600 °C/min	Zr600

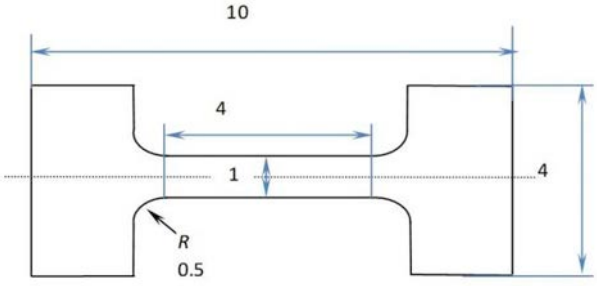

Fig. 1. Tensile bone sample geometry that assures uniform deformation, cross section of 1 × 1 mm^2 [26].

to consolidate the ferritic ODS steel, the use of field assisted sintering techniques (FAST), including Spark plasma sintering (SPS), have been also considered where the powder placed in a graphite die is simultaneously uniaxially pressed and heated by the Joule effect provided by pulses of high intensity current [19–21]. The fast generation of internal heat increases the sintering kinetics giving a minimal grain growth and a rapid densification if a proper final temperature is selected. The uneven characteristics of processed milled powders have provided an heterogeneous recrystallization that lead to a bimodal grain size. In this work it has been studied the effect on final microstructure of the SPS heating rates and the consequences on mechanical properties. Besides, to qualify the material for the use under high temperature, materials, tested using small punch, were compared to GETMAT material project [22,23]. Finally, the strengthening mechanisms contributions at room temperature have been discussed based on strengthening calculations to identify the dominant ones.

2. Experimental procedure

A ferritic ODS steel was obtained by MA and SPS with the composition displayed in Table 1. The starting raw materials were a gas atomized prealloyed powder Fe-14Cr-5Al-3W (wt.%) provided by Sandvik Osprey, pure elemental Ti powder from Gfe mbH, Y_2O_3 nanopowder from TJ Technologies & Materials Inc., and pure elemental Zr powder from Good Fellow.

The MA process was performed in a horizontal attritor (ZOZ CM01) under a constant flow of highly pure Ar atmosphere (99.9995 vol%) with a previous vacuum purge to control the quality of the milled atmosphere. High energy milling was done at 800 rpm with an effective milling time of 2 h. The ball to powder ratio was 20:1. Before the MA process, the powder mixture was mechanically blended for 2 h at 200 rpm.

To monitor the crystallite size and microstrain values evolution (calculated by the Scherrer method) with milling time, the milled powders were characterized by X-ray diffraction. The diffraction patterns were collected on an X'pert Phillips using Cu Kα radiation, with a step size of 0.02° and 7.6 s per step.

To determine the powder shape, morphology and particle size distribution, SEM and laser particle size analyser (Mastersizer 2000) were used.

To consolidate the samples into dense specimens, the processed powders were sintered by Spark Plasma Sintering (SPS) (FCT System GMBH,HPD25,Germany) placed in a graphite die of 20 mm diameter with a final temperature of 1100 °C and a dwell of 5 min under 80 MPa from R.T. The process was done under low vacuum (10^{-2}-10^{-3} mbar) to avoid oxygen enrichment. A tungsten foil (25 μm thickness) was used to cover the die walls and punches to prevent carbon diffusion from the graphite dies/punches into the steel [12,24,25]. The heating rate was modified from 100 to 600 °C/min to tailor the grain size distribution and optimize the densification (Table 2). The temperature was controlled by using a pyrometer in the upper punch. Image analysis (by Jmicrovision® software) was selected for measuring the density of the sintered specimens (at least an area of 868980 μm^2 was considered).

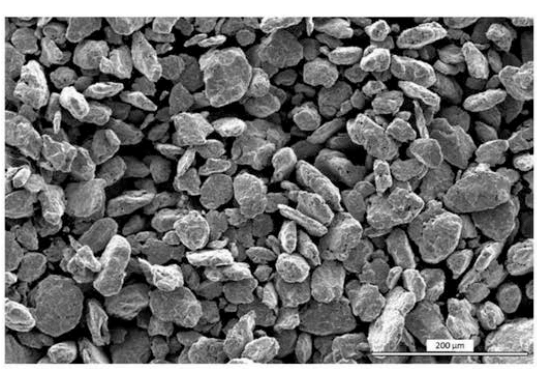

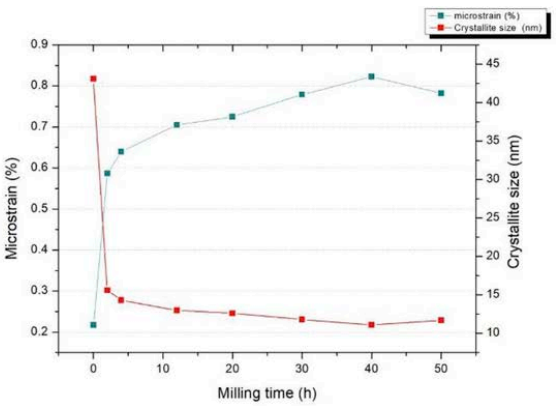

Fig. 2. 14ZrODS powder detail after 50 h of MA, d_{50} = 77 μm (left side). Microstrain and crystallite size evolution during the milling time calculated by Scherrer method on the peak (110) of Fe (right side).

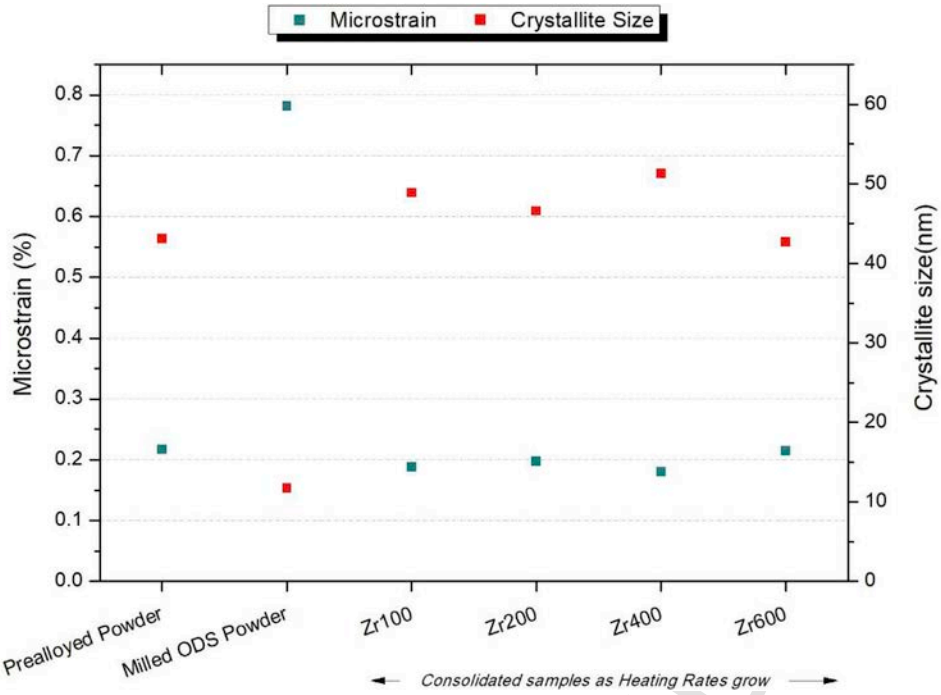

Fig. 3. Microstrain (%) and crystallite size (nm) values in prealloyed/milled powders and after consolidation by SPS at different heating rates.

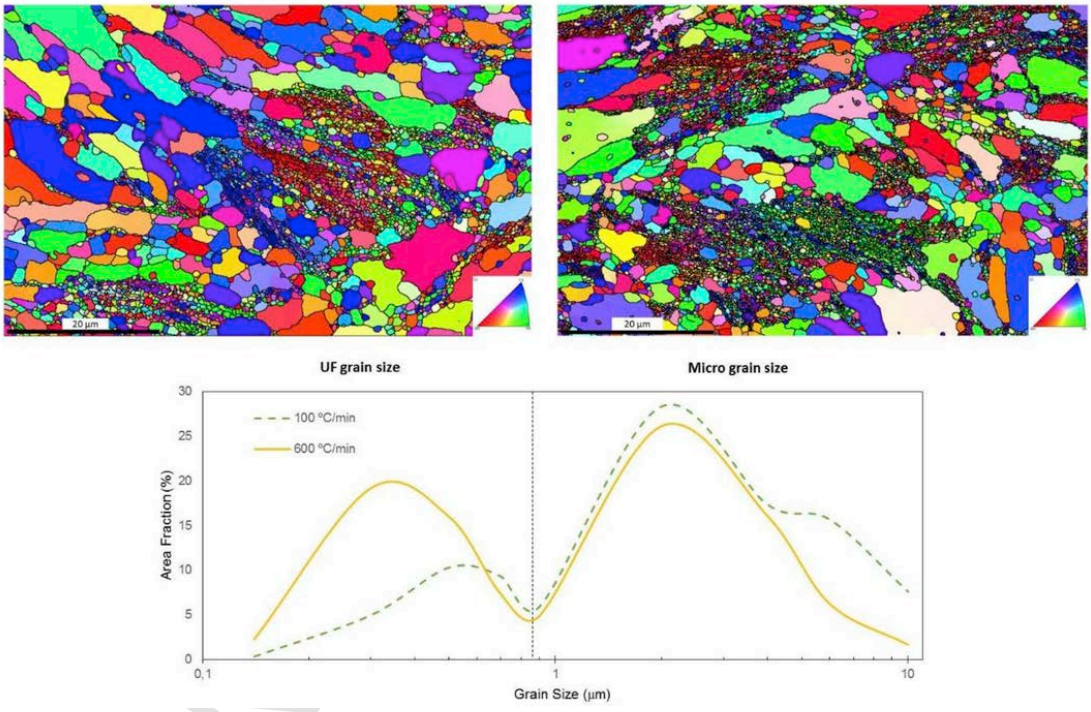

Fig. 4. Zr100 (Left side) and Zr600 (Right side) of the Y IPF (SPS compression direction). Grain size distribution depending on heating rate.

The microstructure was evaluated by SEM (Philips XL-30 and FEI Teneo) and FIB FEG-SEM dual beam microscope coupled to EDX and EBSD detectors (Zeiss Crossbeam 1540). EBSD acquisitions in the transversal section with respect to the compression direction were performed using a step size of 80 nm with a tolerance angle of 2° to determine the grain size distribution.

To assess the mechanical properties, Vickers microhardness $HV_{0.2}$ was measured (200 g load) at R.T (Zwick/Roell ZHVμ model), to evaluate the entire dual microstructure random measurements (20 indentations) were done. R.T tensile response was characterized by miniature specimens (Fig. 1) [26] in a micro tensile machine (Kammrath & Weiss micro machine) with a displacement rate of 2 μm/s, tensile direction is normal to the press direction. To understand the frac-

Table 3
Average grain size, particle size, volume fraction of nanoparticles and dislocation density of the different steels consolidated with different heating rates.

Nomenclature	Zr100	Zr200	Zr400	Zr600
Ultrafine area fraction	19±8	18±6	27±4	32±13
UF grain size (μm)	0.40	0.40	0.39	0.30
Micrograin size (μm)	1.57	1.50	1,51	1.51
Microstrain (%)	0.17	0.15	0.18	0.20
Dislocation density (m^{-2})	6.55 10^{14}	5.10 10^{14}	7.34·10^{14}	9.07·10^{14}

ture behaviour, an in situ SEM observation of microtensile test was also carried out.

To evaluate the mechanical response with temperature, small punch tests were performed at a displacement rate of 0.3 mm/min from R.T. to 500 °C. Discs were prepared from the transverse section to the press direction of the SPS. The specimens (3 mm diameter and 0.250 mm thickness) were finished as mirror-like surfaces to evaluate the fracture mode and ductility.

3. Results

3.1. Characterization, as-milled powder

With the goal of developing nanostructured material after consolidation, it is necessary to start with an MA powder. During MA, the collisions of the grinding media with the initial powder mixture provide the transfer of kinetic energy needed to modify the characteristics of the powder. Subsequent process of plastic deformation causes repeated particles fracturing and cold welding that will condition the progression of the alloying. In this case, after 50 h of effective milling, the powders reached an irregular shape with a diameter (D_{50}) of 77 μm (see Fig. 2 left).

Structural defects or modifications produced during milling, such as solid solution formation, vacancies, dislocations, and stacking faults, will induce an inhomogeneous strain into the crystalline structure. As a result, the lattice distortion increases and the crystalline coherence zone decreases and therefore the crystallite size is reduced [27]. To obtain a nanostructured powder it is necessary to ensure a high microstrain level and low crystallite size as milling time progresses, as show in Fig. 2, right. The minimum crystallite value after 50 h of milling is close to that reported in Ref. [28] for pure Fe, where the minimum average grain size possible by milling was calculated.

The microstrain level will determine the final grain size of the consolidated powders, since the minimum average grain size achieved can be attributed to the balance between the density of dislocations and its recovery by thermal processes, as stated in Ref. [29]. Once a critical level of microstrain is achieved, the crystallite size remains stable, attaining a steady state with milling time. During SPS, the thermal activation will be used first in reducing the strain of the crystallite and then the grain will grow. At the end of MA, even if a steady state is achieved, the plastic deformation stored on each particle is different, as the alloying degree achieved does. In addition, the difference in particle size will have a strong influence on the way in which the material recrystallizes during SPS consolidation.

3.2. Characterization of consolidated samples: effect of heating rate on the final sample

Comparing processed samples with milled ODS powders after the SPS consolidation, the crystallite size and microstrain level change as result of recrystallization during the thermal activation, and consequently the crystallite size increase while the internal strain decreases (Fig. 3) [30]. At the end, the values are close to those obtained for the starting prealloyed grade powder, which has a fine grain microstruc-

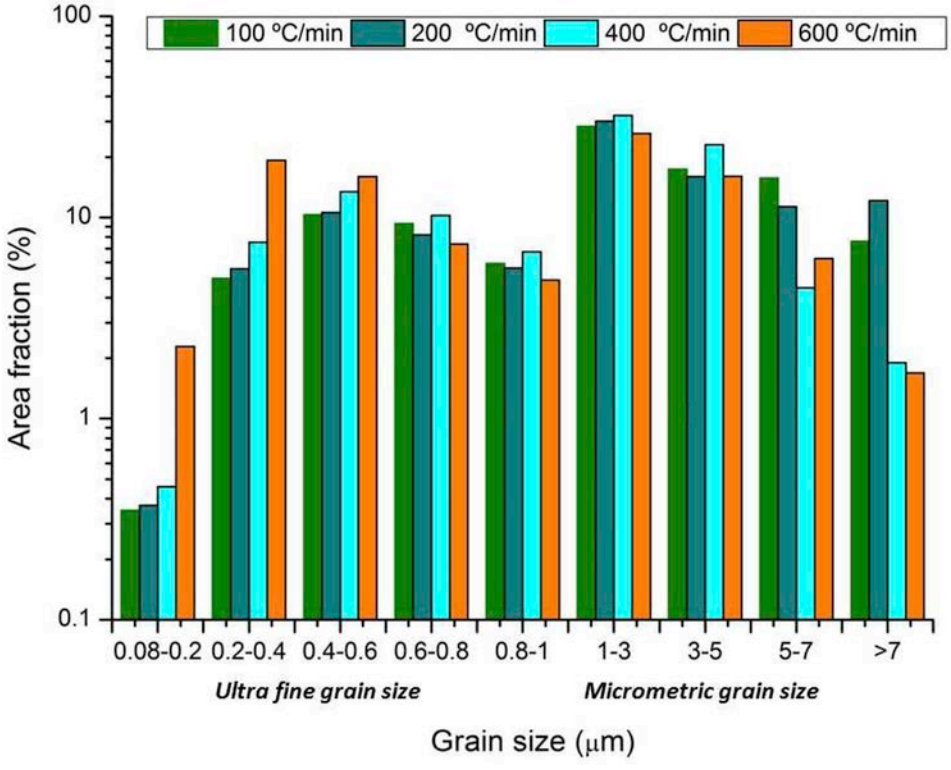

Fig. 5. Grain size distribution by using different heating rates: ultrafine grain size (from 0.08 to 0.8), and micrometric grain size (from 0.8).

Table 4
Samples densities using different heating rates (%).

Nomenclature	Zr100	Zr200	Zr400	Zr600
Density (%)	99.4±0.5	99.2±0.5	98.7±0.2	98.6±0.1

ture due to the fast cooling rate applied during the gas atomization process.

In the course of the sintering process, independently of the heating rate, each individual powder particle recovers and recrystallizes in a different degree, following an inhomogeneous recrystallization. As a consequence, the sintered ODS steel evolves into a dual grain size microstructure comprising colonies of ultrafine (UF) grains and colonies of micro size grains. As the heating rate increases, the area taken up by the ultrafine colonies is greater and, at the same time, the mean grain size decreases (Fig. 4).

A total area of 9000 μm^2 per SPS sample was considered for the statistical analysis. The effect of the heating rate on the extension of the ultrafine grain areas is especially clear for heating rates above 400 °C/min (Table 3).

Higher heating rates have a direct effect not only on the presence of ultrafine areas in the material but also in the average grain size inside those areas, reducing them as soon as the heating rate is increased. On the other hand, the micrometric grain is also affected. The average micrometric grain size in this region is also reduced, or at least maintained, when the heating rate is increased (Fig. 5). Fine grains combined with micrometric grains could demonstrate a special mechanical behaviour, providing good toughness without strength loss [31].

To evaluate this phenomenon dislocation density was calculated by using X-ray diffraction through the next equation (1):

$$\rho = 14.4\frac{\varepsilon^2}{b^2} \quad (1)$$

Trying to perform a more accurate measurement the microstrain (ε) was calculated by means of Williamson-Hall equation [32]. Higher dislocation densities were achieved when 600 °C/min heating rate is selected (Table 3).

In the literature, it is reported how the heating rate could also have an effect on the final densification of the material, increasing it as soon as the heating rate is increased [33,34]. In this case, the equilibrium achieved between temperature and pressure has the largest effect on the final consolidation. The final densities achieved are almost the same independent of the heating rate used (Table 4).

3.3. Evaluation of mechanical properties

3.3.1. Microhardness

The materials' resistance to local plastic deformation was tested by microhardness. Fig. 6 shows how the consolidated ODS steels with Zr additions have reached a level comparable to ODS RAF consolidated by a more complex processing route (HIP plus thermomechanical treatment) [35]. The reduction of the grain size, the precipitation of new nano-oxides and the efficient solid solution strengthening leads to an increase in the hardness obtained. These values are of the same order as those reported in the literature [17,36].

Considering the relationship between hardness and strength, where HV ~3 σ (transfer HV to Pa) [37] it is possible to estimate the yield strength of these ODS sintered steels (assuming σ as σy) since they have exhibited strain hardening (Table 5).

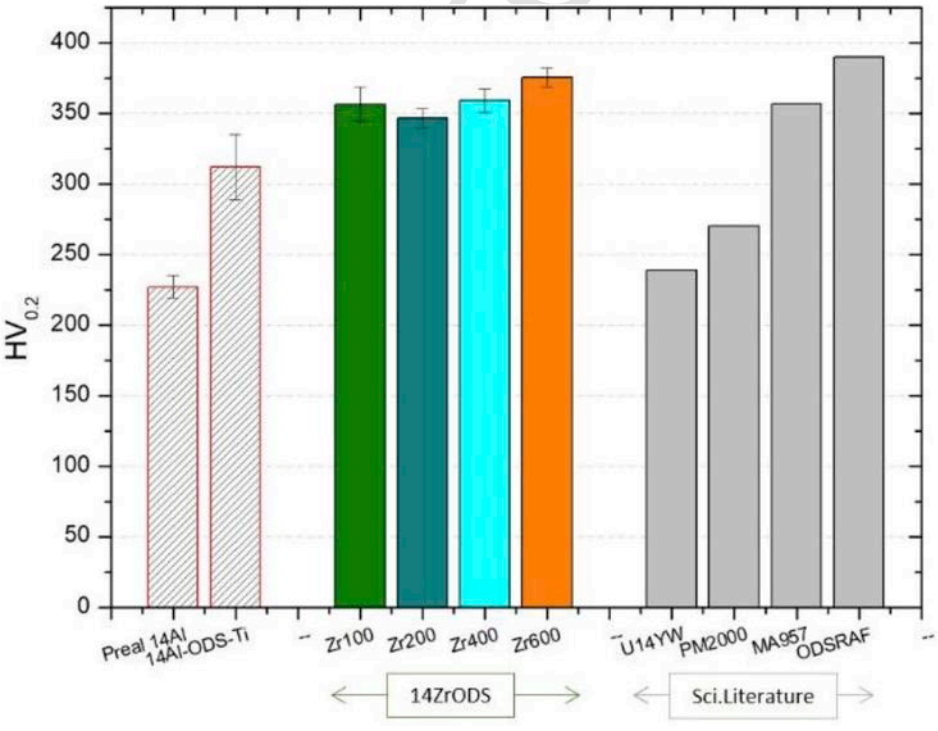

Fig. 6. Microhardness of different ODS steels.

Table 5
Yield Strength evaluated by microhardness.

Nomenclature	Zr100	Zr200	Zr400	Zr600
σ_y (MPa)	1163	1132	1172	1226

3.3.2. Tensile performance

Independent of the heating rate used, 14ZrODS steels have demonstrated extraordinary UTS values (Fig. 7) particularly when Zr600 is considered. This ODS has shown the higher fraction area of ultrafine grains and the lower grain size distribution inside them. Values obtained by the previous estimation using microhardness data (Table 5) show the same trend obtained by tensile tests especially on the Yield Strength.

Toughness is essentially affected by the final density and by the balance of ultrafine grains to micrometric grains as well. Although all the consolidated materials, from Zr100 to Zr600, present a good equilibrium between toughness and UTS, the higher results are achieved again for the material processed at 600 °C/min which exhibit the largest area of colonies with ultrafine grains.

The in situ tests help to understand the mechanical behaviour of these ODS steels (Fig. 7). Cracks appear at 45° with respect the load applied. This phenomenon, together with the necking on the sample in the gauge section, proves the ductility of the material.

3.3.3. Small punch test

The results of the SP tests are represented in the load-deflection curves (Fig. 8). The mechanical behaviour of the material is clearly determined by the Zr addition. The bimodal microstructure obtained by the 14ZrODS, together with the pinning effect of the nano-oxides presented on the material, makes the differences with the 14Al-ODS-Ti steel (Zr-free).

It is worth mentioning the effect of heating rate, the Zr600 ODS steel maintains the maximum load until 300 °C, at which point it starts to descend. The response of this processed material Zr600 in terms of ductility (deflection) and maximum load (F_m) is comparable to that observed for the hot extruded ODS steel analysed in GETMAT project (Fig. 8).

Fractography of the SP tested specimens has shown two different behaviours (Fig. 9) regardless the processing conditions. A typical ductile-fragile fracture mode with open and circumferentially ori-

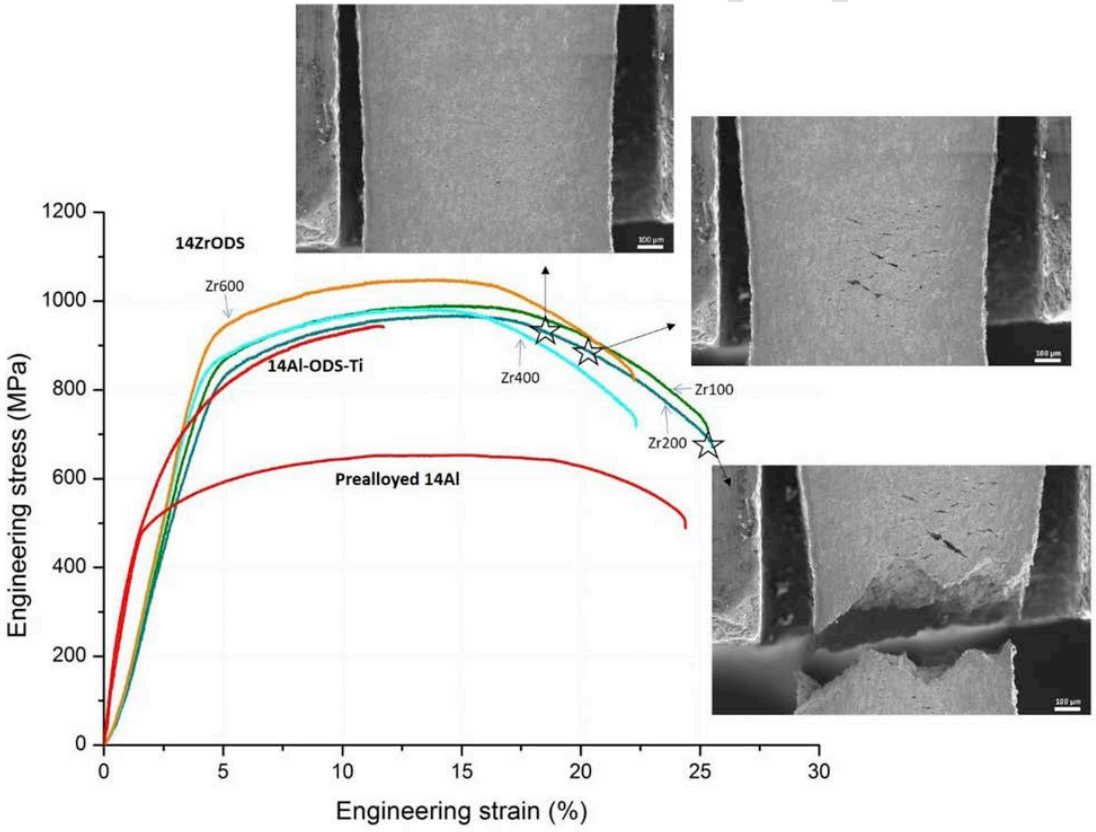

	UTS (MPa)	YS (MPa)	Toughness (MPa)	Total Deformation (%)
Zr100	976 ± 14	811 ± 15	197 ± 10	25.0 ± 2.3
Zr200	960 ± 3	802 ± 6	207 ± 2	25.8 ± 0.3
Zr400	973 ± 9	832 ± 10	192 ± 9	23.6 ± 1.1
Zr600	1040 ± 10	910 ± 10	195 ± 9	22.4 ± 0.8

Fig. 7. Comparison of engineering tensile stress-strain curves for the SPSed ODS steels. SEM micrographs showing the cracks formed during the tensile test of Zr200 ODS steel depending on tensile deformation.

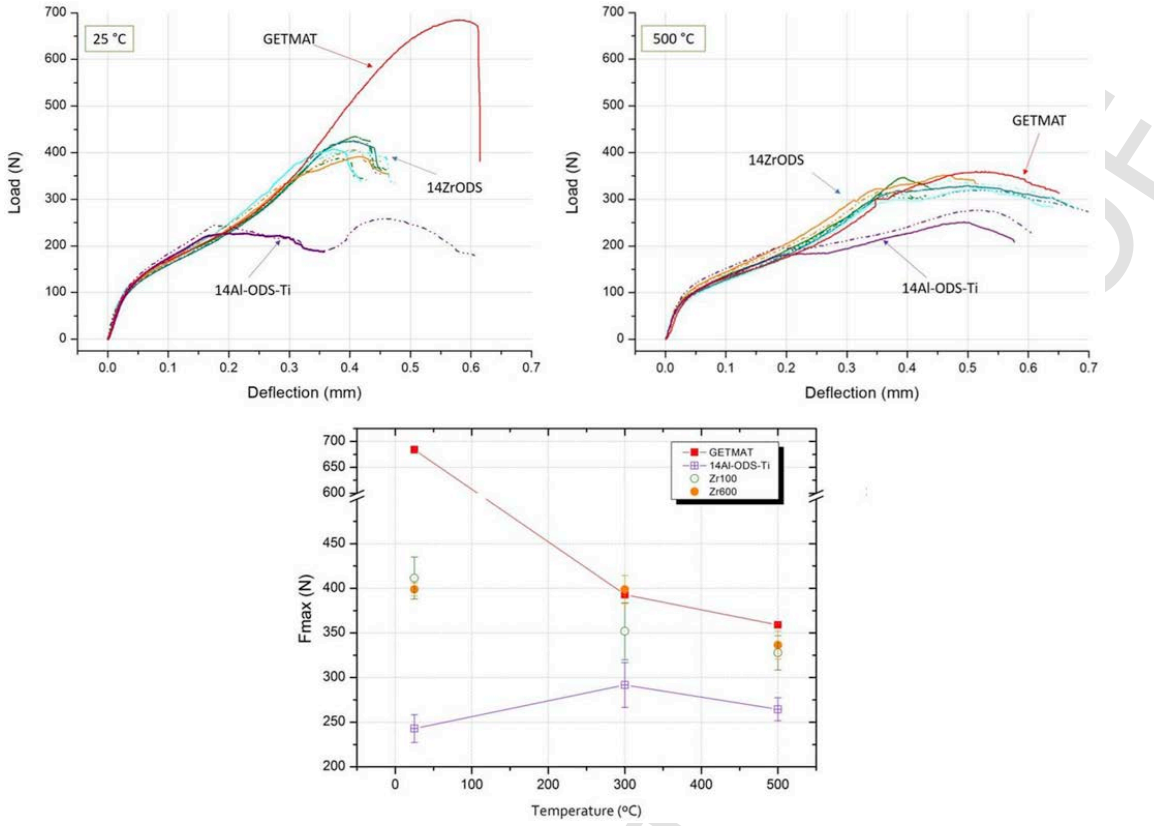

Fig. 8. Small punch test at RT and 500 °C and maximum load values achieved at different temperatures.

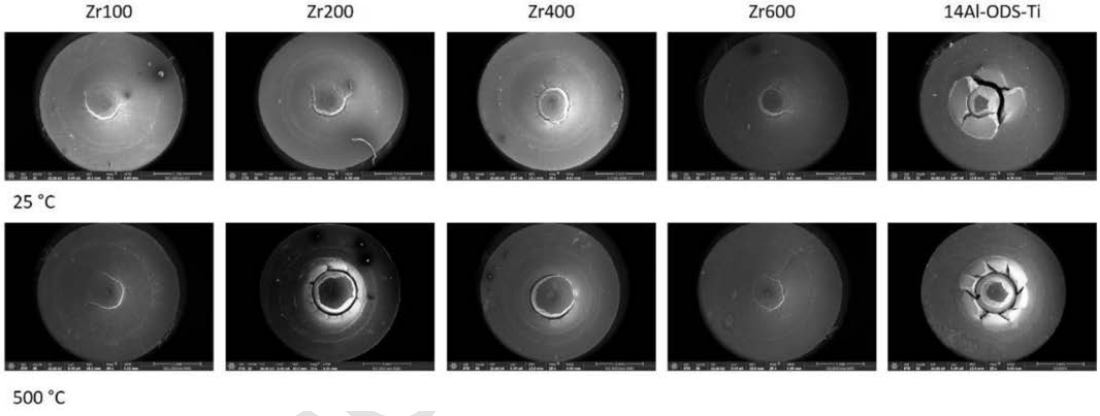

Fig. 9. Small Punch fracture specimens.

ented cracks for the 14ZrODS group, and a fragile fracture mode with radial cracks in the case of Zr-free ODS steel −14Al-ODS-Ti [23,38].

4. Discussion

4.1. Influence of processing conditions

The sintered ODS steel evolves into a dual grain size microstructure comprising colonies of ultrafine (UF) grains and colonies of micro size grains. Three parameters control the grain growth [20]. First, the nano-oxide precipitation, which produces a strong pinning effect on the grain boundaries that will transform into an abnormal growth, which affects the final microstructure [39]. Second, the unequal plastic deformation and alloying distribution achieved during the MA will determine the stored energy and the ability of recrystallization [39–41]. Finally, faster heating rates involve the increase of the current intensity. Therefore, the heating generated by the Joule effect on particles increases as well. At the same time, the high density of lattice defects decreases the conductivity of the initial powder, limiting the penetration depth of the Joule effect. Consequently, there is a temperature gradient on the former particle. Hence, grains close to the particle surface have higher probability to recrystallize, leading into abnormal growth [42–44].

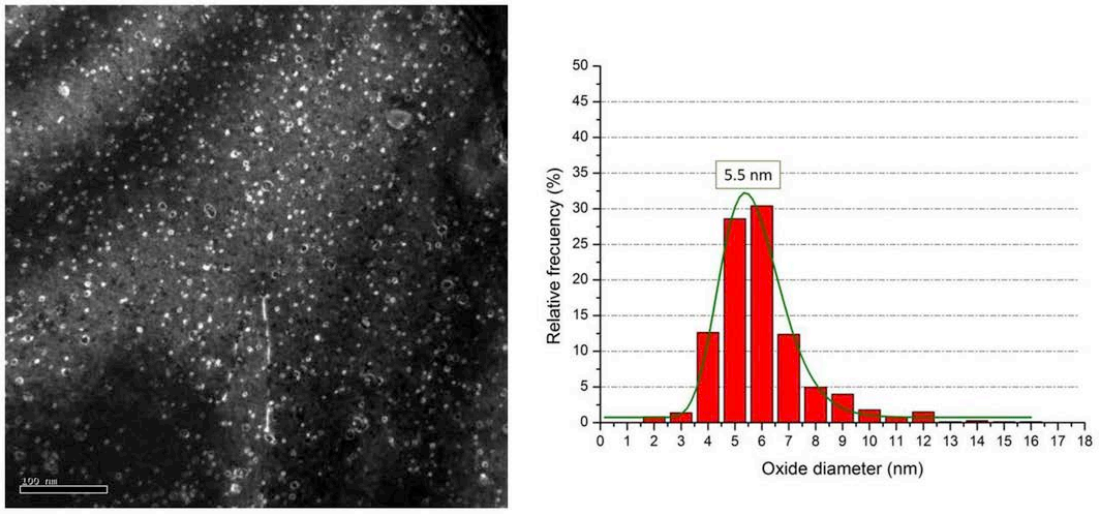

Fig. 10. Nano oxides precipitates on Zr600 samples, Weak Beam Dark Field (WBDF) TEM.

Table 6
Yield strength value experimentally obtained and strengthening calculated by theoretical contribution (in MPa).

Nomenclature	Zr100	Zr200	Zr400	Zr600
σ_{gb}	268	271	288	339
σ_{dislo}	559	493	592	657
σ_{p}	205	205	205	205
$\sigma_{y,calc}$	1057	999	1108	1221
$\sigma_{y,experimental}$	811	802	832	910

This uneven recrystallization was also observed when the MA powder is consolidated by HIP, which implies higher thermal activation and longer consolidation times. (i.e. 1150 °C, 200 MPa, 2–4 h) [20,45]. Differences of SPS and HIP consolidation arrive when ultrafine colonies are measured, in case of SPS they covers larger areas [46], further, the grain size distribution inside those ultrafine colonies is smaller. The shorter thermal history when samples are heated at 600 °C/min has a strong effect on the final microstructure achieved (Fig. 4) keeping higher dislocation density than the others processed ODS.

Consolidation time and temperature directly affect the grain growth, so limiting the time for sintering selecting SPS could be a key-factor.

4.2. Strengthened mechanisms

Changes produced on the microstructure are not clearly observable on the final mechanical properties achieved and only when the

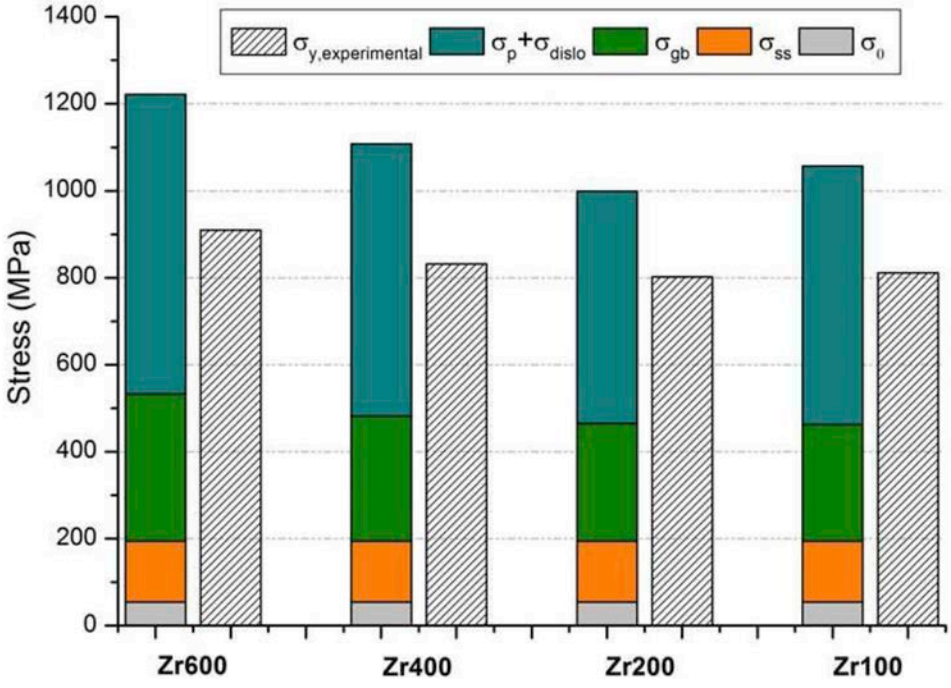

Fig. 11. Experimental and estimated yield strength at room temperature.

Table 7
Comparison of theoretical contribution (in MPa) considering two approach vs experimental results.

Nomenclature	Zr100	Zr200	Zr400	Zr600
$\sigma_{y,calc} = f(\sigma_0, \sigma_{ss}, \sigma_{gb}, \sigma_{dis}, \sigma_p)$	1057	999	1108	1221
$\sigma'_{y,calc} = f(\sigma_{gb}, \sigma_{dis}, \sigma_p)$	863	805	914	1028
$\sigma_{y,experimental}$	811	802	832	910

heating rate selected is 600 °C/min, remarkable difference could be appreciated. For this reason, to clarify the contribution of the different strengthening methods is mandatory. For this purpose, equation (2) is used following the reported results in other works [32,47–49]:

$$\sigma_y = \sigma_0 + \sigma_{ss} + \sigma_{gb} + \sqrt{\sigma_{dis}^2 + \sigma_p^2} \quad (2)$$

where σ_y is the yield strength of ODS steel and σ_0 is the lattice friction stress of pure iron whose value was taken as 53.9 MPa [49].

The σ_{ss} is the solid solution contribution. First, the solid solution strengthening can be divided into the interstitial strengthening and into substitutional strengthening. In this work, it is assume that the input of Ti, Al or Zr to solid solution strengthening or the one provided by C or N due to the milling step are negligible, so it can be neglected. Cr and W are the main alloying elements providing this strengthening. This parameter is given by equation (3) [50]:

$$ff_{ss} = 0.00689 \sum K_i \cdot c_i^z \quad (3)$$

Where k is the strengthened coefficient and c_i is the atomic percent of the different substitutional elements, such as Cr or W. As it is stated in Refs. [49,50] the value of K_i for Cr is 1400 and for W is 11000 and for the substitutional elements the exponent z is equal to 0.75 as stated in Refs. [32,47,48]. In this work, the atomic percentage of Cr is 14%, and it is 0.83% for W, which gives a total value of 140 MPa.

The strengthening of grain boundaries can be described as a dual material in which the different regions, depending on the grain growth, are going to provide different levels of strength as a function of their grain size, following equation (4) [51]:

$$ff_{gb} = f \cdot \left(\frac{1}{5} G \sqrt{\frac{b}{d_g}}\right) \quad (4)$$

Equation (4) was slightly modified adding f which represent the area faction covered by ultra fine or micrometric grain size, trying to perform an accurate measurement as it was proposed in Ref. [48]. G is the iron shear modulus (85 GPa) [52], b is the burger vector (0.252 nm). Tailoring the right microstructure has a direct effect on this parameter.

The dislocation hardening was calculated by equation (5) [53]:

$$ff_{dislo} = {}_{,d} MGb\sqrt{j} \quad (5)$$

Where M is the Taylor factor (3.06) [54], α_d is a constant (1/3) [51], and ρ is the dislocation density. Table 3 summarizes all the parameters necessary to perform this calculation.

Finally, the oxide contribution usually was estimated by the Orowan bypass mechanism [32].However, this theory supposed that the oxides particles are impenetrable without taken into account the range of coherency of the different oxides. Chauhan et all [49] proposed the use of another equation based on the formulation of Seeger [55,56]:

$$\sigma_p = \alpha_p MGb\sqrt{N_p d_p} \quad (6)$$

Where α_p is the obstacle strength for oxide nanoparticles which could vary from 0.1 to 0.5 (depending on the particle type and the degree of coherency). Following the parameters used by Chauhan et all in Ref. [49], α_p was taken as 1/3. Besides, N_p represent the density of nano-oxides and d_p is the mean particle diameter, which was determined by TEM observation (Fig. 10). In a ODS steel by refining the size and increasing the oxide volume fraction is possible to increase the contribution of that term σ_p. As the heating rate does not show an effect on the oxide precipitation, the system was simplified assuming the same volume fraction and mean oxide diameters for each material. If the mean oxide size is 5.5 nm and the precipitation density is $1.63 \cdot 10^{22} m^{-3}$, then the volume fraction is 0.142%. This gives a contribution by precipitation hardening of 205 MPa.

The input of each term of eq. (2) is gathered in Table 6. The theoretical calculations highlight that the grain size has a small influence on the final yield strength (see Fig. 11). However, the dual grain size distribution has shown a greater influence for balancing the mechanical response, allowing a higher strain level in the processed ODS steel.

The processed ODS material is specially conditioned by the hardening produced by the dislocation density and particle pinning, which plays the main role between the strengthening mechanisms.

The difference between experimental results and theoretical calculations could be due to the strengthened promoted by lattice friction and solid solution hardening. Lattice fiction stress depends directly on the type of dislocation slip system and temperature, for this reason, friction stress value could suffer modifications [57]. Apart from that, Cr and W contents determine the solid solution strengthening term, but both elements form carbides along the material which could lead to a decrease of the real combined amount in solid solution [58]. Hence, the σ_{ss} value could be lower. If these two terms are neglected and it is only considered as dominant the contributions of σ_{gb}, σ_{dislo} and σ_p, the theoretical calculation has shown a superior exactitude with regards to experimental data as stated in Ref. [49] (Table 7).

4.3. Evaluation of the material under high temperature

The results of the small punch tests suggest small differences with the variation of the heating rate from room temperature to 500 °C, making the grain refinement insufficient to be detected by this method [59]. Independently of the heating rate used, all the materials processed are hardened by dislocation density and oxides precipitation. Both terms allow those materials to present a stable behaviour under high temperature service. It is assumed from previous studies performed at high temperature that until 400 °C, the contribution to the strengthening produced by the dislocations is constant. Solid solutions follow the same path but until 600 °C [48]. This explain why at 500 °C there is a drop in the mechanical properties (F_{max}) since the dislocation density seems to be reduced at this temperature [48]. What is not clear is the effect of the precipitates at high temperatures. Nano-oxides present high thermal stability, avoiding the coarsening at temperatures near to $0{,}8T_{s,}$ where T_s is the solidus temperature of the alloy [20]. If those oxides are refined by Zr addition [7,9,11,60–64] and coherent oxides are obtained, the pinning effect at

high temperature could be maintained and it allows the material to present good properties under those conditions.

Then, the Zr addition is the key-factor in the improvement of the mechanical properties at high temperature.

The SP results show how this ODS steel is comparable to the one studied in the GETMAT project (manufactured under a more complex route) at least in terms of yield behaviour [22,23].

5. Conclusions

In this research, an ODS steel has been developed by the addition of Zr, and it has been successfully processed by using SPS as a consolidation technique. It is demonstrated that:

- The selection of the SPS processing conditions can modify the grain size distribution. By fixing an optimum heating rate, a large effect on the grain size is obtained. Higher heating rates increase the area of ultra-fine regions and reduce the grain size inside these areas, while the micrometric grain coarsening is reduced.
- The best values of microhardness and UTS are achieved for the material consolidated at 600 °C/min. Although the grain refinement contributes to the increase of these properties, it is not the main factor affecting the mechanical behaviour. Dislocation and oxide hardening are the factors that determine the final mechanical properties. Small punch tests demonstrate how Zr600 can keep the maximum load until 300 °C. However, at 500 °C, Zr100 and Zr600 have almost the same behaviour.
- However, Zr addition has the strongest effect on improving the mechanical behaviour of the material, offering an extraordinary balance between toughness and UTS and also good properties at high temperatures (500 °C).
- The analysis of the mechanical properties proves that SPS ODS steels with Zr have similar characteristic to the ones obtained by traditional consolidation method such as HIP or HE.

Data availability statement

The raw/processed data required to reproduce these findings cannot be shared at this time as the data also forms part of an ongoing study. However if they are required I would be able to provide all the data afterwards by just contact by email: eric.macia@uc3m.es.

Acknowledgements

Authors want to acknowledge Ferro-Ness project and Ferro-Genesys project funded by MINECO under National I + D + I program MAT2016-80875-C3-3-R and MAT2013-47460-C5-5-P. The authors gratefully acknowledge the help received from Daniel Plaza during the Small-Punch tests.

References

[1] K. Rajan, V.S. Sarma, T.R.G. Kutty, B.S. Murty, Hot hardness behaviour of ultrafine grained ferritic oxide dispersion strengthened alloys prepared by mechanical alloying and spark plasma sintering, Mater. Sci. Eng. A 558 (2012) 492–496, https://doi.org/10.1016/j.msea.2012.08.033.

[2] C.-L. Chen, A. Richter, R. Kögler, G. Talut, Dual beam irradiation of nanostructured FeCrAl oxide dispersion strengthened steel, J. Nucl. Mater. 412 (2011) 350–358, https://doi.org/10.1016/j.jnucmat.2011.03.041.

[3] S. Ukai, T. Nishida, H. Okada, Development of ODS ferritic steels for FBR core application , (I), J. Nulcear Sci. Technol. 34 (1997) 256–263.

[4] H. Zhang, Y. Huang, H. Ning, C.A. Williams, A.J. London, K. Dawson, Z. Hong, M.J. Gorley, C.R.M. Grovenor, G.J. Tatlock, S.G. Roberts, M.J. Reece, H. Yan, P.S. Grant, Processing and microstructure characterisation of oxide dispersion strengthened Fe–14Cr–0.4Ti–0.25Y2O3 ferritic steels fabricated by spark plasma sintering, J. Nucl. Mater. 464 (2015) 61–68, https://doi.org/10.1016/j.jnucmat.2015.04.029.

[5] S. Ukai, S. Mizuta, M. Fujiwara, T. Okuda, T. Kobayashi, Development of 9cr-ods martensitic steel claddings for fuel pins by means of ferrite to austenite phase transformation, J. Nucl. Sci. Technol. 39 (2002) 778–788, https://doi.org/10.1080/18811248.2002.9715260.

[6] J. Isselin, R. Kasada, A. Kimura, T. Okuda, M. Inoue, S. Ukai, S. Ohnuki, T. Fujisawa, F. Abe, Effects of Zr addition on the microstructure of 14%Cr4%Al ODS ferritic steels, Mater. Trans. 51 (2010) 1011–1015, https://doi.org/10.2320/matertrans.MBW200923.

[7] P. Dou, A. Kimura, R. Kasada, T. Okuda, M. Inoue, S. Ukai, S. Ohnuki, T. Fujisawa, F. Abe, TEM and HRTEM study of oxide particles in an Al-alloyed high-Cr oxide dispersion strengthened steel with Zr addition, J. Nucl. Mater. 444 (2014) 441–453, https://doi.org/10.1016/j.jnucmat.2013.10.028.

[8] A. Yabuuchi, M. Maekawa, A. Kawasuso, Influence of oversized elements (Hf, Zr, Ti and Nb) on the thermal stability of vacancies in type 316L stainless steels, J. Nucl. Mater. 430 (2012) 190–193, https://doi.org/10.1016/j.jnucmat.2012.07.005.

[9] W. Li, T. Hao, R. Gao, X. Wang, T. Zhang, Q. Fang, C. Liu, The effect of Zr, Ti addition on the particle size and microstructure evolution of yttria nanoparticle in ODS steel, Powder Technol. 319 (2017) 172–182, https://doi.org/10.1016/J.POWTEC.2017.06.041.

[10] R. Gao, T. Zhang, X.P. Wang, Q.F. Fang, C.S. Liu, Effect of zirconium addition on the microstructure and mechanical properties of ODS ferritic steels containing aluminum, J. Nucl. Mater. 444 (2014) 462–468, https://doi.org/10.1016/j.jnucmat.2013.10.038.

[11] Haijian Xu, Z. Lua, D. Wanga, C. Liu, Effect of zirconium addition on the microstructure and mechanical properties of 15Cr-ODS ferritic Steels consolidated by hot isostatic pressing, Fusion Eng. Des. 114 (2017) 33–39, https://doi.org/10.1016/J.FUSENGDES.2016.11.011.

[12] A. García-Junceda, N. García-Rodríguez, M. Campos, M. Cartón-Cordero, J.M. Torralba, Effect of zirconium on the microstructure and mechanical properties of an Al-alloyed ODS steel consolidated by FAHP, J. Am. Ceram. Soc. 98 (2015) 3582–3587, https://doi.org/10.1111/jace.13691.

[13] C.Z. Yu, H. Oka, N. Hashimoto, S. Ohnuki, Development of damage structure in 16Cr–4Al ODS steels during electron-irradiation, J. Nucl. Mater. 417 (2011) 286–288, https://doi.org/10.1016/j.jnucmat.2011.02.037.

[14] H. Kishimoto, R. Kasada, A. Kimura, M. Inoue, T. Okuda, F. Abe, S. Ohnuki, T. Fujisawa, No titleIn: Proc. ICAPP 2009, 2009.

[15] S. Ohnuki, N. Hashimoto, S. Ukai, A. Kimura, M. Inoue, T. Kaito, T. Fujisawa, T. Okuda, F. Abe, A. Kimura, No titleIn: Proc. ICAPP, 2009.

[16] N. García-Rodríguez, M. Campos, J.M. Torralba, M.H. Berger, Y. Bienvenu, Capability of mechanical alloying and SPS technique to develop nanostructured high Cr, Al alloyed ODS steels, Mater. Sci. Technol. 30 (2014) 1676–1684, https://doi.org/10.1179/1743284714Y.0000000595.

[17] Z. Oksiuta, N. Baluc, Effect of mechanical alloying atmosphere on the microstructure and Charpy impact properties of an ODS ferritic steel, J. Nucl. Mater. 386–388 (2009) 426–429, https://doi.org/10.1016/j.jnucmat.2008.12.148.

[18] Z. Oksiuta, P. Hosemann, S.C. Vogel, N. Baluc, Microstructure examination of Fe-14Cr ODS ferritic steels produced through different processing routes, J. Nucl. Mater. 451 (2014) 320–327, https://doi.org/10.1016/j.jnucmat.2014.04.004.

[19] M.A. Auger, V. De Castro, T. Leguey, A. Muñoz, R. Pareja, Microstructure and mechanical behavior of ODS and non-ODS Fe-14Cr model alloys produced by spark plasma sintering, J. Nucl. Mater. 436 (2013) 68–75, https://doi.org/10.1016/j.jnucmat.2013.01.331.

[20] X. Boulnat, M. Perez, D. Fabregue, T. Douillard, M.H. Mathon, Y. De Carlan, Microstructure evolution in nano-reinforced ferritic steel processed by mechanical alloying and spark plasma sintering, Metall. Mater. Trans. A Phys. Metall. Mater. Sci. 45 (2014) 1485–1497, https://doi.org/10.1007/s11661-013-2107-y.

[21] P. Franke, C. Heintze, F. Bergner, T. Weißgärber, Mechanical properties of spark plasma sintered Fe-Cr compacts strengthened by nanodispersed yttria particles, Mater. Test. 52 (2010) 133–138, https://doi.org/10.3139/120.110115.

[22] M. Serrano, M. Hernández-Mayoral, A. García-Junceda, Microstructural anisotropy effect on the mechanical properties of a 14Cr ODS steel, J. Nucl. Mater. 428 (2012) 103–109, https://doi.org/10.1016/j.jnucmat.2011.08.016.

[23] M. Serrano, A. García-Junceda, R. Hernández, M.H. Mayoral, On anisotropy of ferritic ODS alloys, Mater. Sci. Technol. 30 (2014) 1664–1668, https://doi.org/10.1179/1743284714Y.0000000552.

[24] B.B. Bokhonov, A.V. Ukhina, D.V. Dudina, A.G. Anisimov, V.I. Mali, I.S. Batraev, Carbon uptake during Spark Plasma Sintering: investigation through the analysis of the carbide “footprint” in a Ni–W alloy, RSC Adv. 5 (2015) 80228–80237, https://doi.org/10.1039/C5RA15439A.

[25] A. García-Junceda, L. Acebo, J.M. Torralba, Study and suppression of the microstructural anisotropy generated during the consolidation of a carbonyl iron powder by field-assisted hot pressing, Metall. Mater. Trans. A Phys. Metall. Mater. Sci. 46 (2015) 3192–3198, https://doi.org/10.1007/s11661-015-2919-z.

[26] Y.H. Zhao, Y.Z. Guo, Q. Wei, T.D. Topping, A.M. Dangelewicz, Y.T. Zhu, T.G. Langdon, E.J. Lavernia, Influence of specimen dimensions and strain measure-

ment methods on tensile stress-strain curves, Mater. Sci. Eng. A 525 (2009) 68–77, https://doi.org/10.1016/j.msea.2009.06.031.
[27] J.M. Torralba, L. Fuentes-Pacheco, N. García-Rodríguez, M. Campos, Development of high performance powder metallurgy steels by high-energy milling, Adv. Powder Technol. 24 (2013) 813–817, https://doi.org/10.1016/j.apt.2012.11.015.
[28] F.A. Mohamed, Y. Xun, Correlations between the minimum grain size produced by milling and material parameters, Mater. Sci. Eng. A 354 (2003) 133–139, https://doi.org/10.1016/S0921-5093(02)00936-X.
[29] J. Eckert, J. Holzer, C. E.Krill III, W. Johnson, C. Krill, W. Johnson, Structural and thermodynamic properties of nanocrystalline fcc metals prepared by mechanical attrition, J. Mater. Res. 7 (1992) 1751–1761, https://doi.org/10.1557/JMR.1992.1751.
[30] M. Perez, Y. De Carlan, J.L. Be, D. Fabre, N. Sallez, X. Boulnat, A. Borbe, Y. Bre, L. Hennet, C. Mocuta, D. Thiaudie, ScienceDirect in Situ Characterization of Microstructural Instabilities : Recovery , Recrystallization and Abnormal Growth in Nanoreinforced Steel Powder, vol. 87, 2015377–389, https://doi.org/10.1016/j.actamat.2014.11.051.
[31] X. Wu, Y. Zhu, Heterogeneous materials: a new class of materials with unprecedented mechanical properties, Mater. Res. Lett. 5 (2017) 527–532, https://doi.org/10.1080/21663831.2017.1343208.
[32] J. Shen, Y. Li, F. Li, H. Yang, Z. Zhao, S. Kano, Y. Matsukawa, Y. Satoh, H. Abe, Microstructural characterization and strengthening mechanisms of a 12Cr-ODS steel, Mater. Sci. Eng. A 673 (2016) 624–632, https://doi.org/10.1016/j.msea.2016.07.030.
[33] I. Bogachev, E. Grigoryev, O.L. Khasanov, E. Olevsky, Fabrication of 13Cr-2Mo ferritic/martensitic oxide-dispersion-strengthened steel components by mechanical alloying and spark-plasma sintering, JOM (J. Occup. Med.) 66 (2014) 1020–1026, https://doi.org/10.1007/s11837-014-0972-5.
[34] M.S. Staltsov, I.I. Chernov, I.A. Bogachev, B.A. Kalin, E.A. Olevsky, L.J. Lebedeva, A.A. Nikitina, Optimization of mechanical alloying and spark-plasma sintering regimes to obtain ferrite–martensitic ODS steel, Nucl. Mater. Energy (2016) https://doi.org/10.1016/j.nme.2016.08.020.
[35] Z. Oksiuta, N. Baluc, Optimization of the chemical composition and manufacturing route for ODS RAF steels for fusion reactor application, Nucl. Fusion 49 (2009) https://doi.org/10.1088/0029-5515/49/5/055003.
[36] M.J. Alinger, G.R. Odette, D.T. Hoelzer, On the role of alloy composition and processing parameters in nanocluster, Fusion Mater. Semiannu. Prog. Rep. (2008) 53–78.
[37] P. Zhang, S.X. Li, Z.F. Zhang, General relationship between strength and hardness, Mater. Sci. Eng. A 529 (2011) 62–73, https://doi.org/10.1016/j.msea.2011.08.061.
[38] K. Guan, L. Hua, Q. Wang, X. Zou, M. Song, Assessment of toughness in long term service CrMo low alloy steel by fracture toughness and small punch test, Nucl. Eng. Des. 241 (2011) 1407–1413, https://doi.org/10.1016/j.nucengdes.2011.01.031.
[39] X. Boulnat, N. Sallez, M. Dadé, A. Borbély, J. Béchade, Y. De Carlan, J. Malaplate, Acta Materialia Influence of oxide volume fraction on abnormal growth of nanostructured ferritic steels during non-isothermal treatments : an in situ study, Acta Mater. 97 (2015) 124–130, https://doi.org/10.1016/j.actamat.2015.07.005.
[40] M. Dadé, J. Malaplate, J. Garnier, F. De Geuser, N. Lochet, A. Deschamps, Influence of consolidation methods on the recrystallization kinetics of a Fe-14Cr based ODS steel, J. Nucl. Mater. 472 (2016) https://doi.org/10.1016/j.jnucmat.2016.01.019.
[41] N. Sallez, C. Hatzoglou, F. Delabrouille, D. Sornin, L. Chaffron, M. Blat-Yrieix, B. Radiguet, P. Pareige, P. Donnadieu, Y. Bréchet, Precipitates and boundaries interaction in ferritic ODS steels, J. Nucl. Mater. 472 (2016) 118–126, https://doi.org/10.1016/j.jnucmat.2016.01.021.
[42] R. Xie, Z. Lu, C. Lu, Z. Li, X. Ding, C. Liu, Microstructures and mechanical properties of 9Cr oxide dispersion strengthened steel produced by spark plasma sintering, Fusion Eng. Des. 115 (2017) 67–73, https://doi.org/10.1016/j.fusengdes.2016.12.034.
[43] K. Vanmeensel, A. Laptev, J. Hennicke, J. Vleugels, O. Van Der Biest, Modelling of the temperature distribution during field assisted sintering, Acta Mater. 53 (2005) 4379–4388, https://doi.org/10.1016/j.actamat.2005.05.042.
[44] U. Anselmi-Tamburini, S. Gennari, J.E. Garay, Z.A. Munir, Fundamental investigations on the spark plasma sintering/synthesis process: II. Modeling of current and temperature distributions, Mater. Sci. Eng. A 394 (2005) 139–148, https://doi.org/10.1016/j.msea.2004.11.019.
[45] M.A. Auger, T. Leguey, A. Muñoz, M.A. Monge, V. de Castro, P. Fernández, G. Garcés, R. Pareja, Microstructure and mechanical properties of ultrafine-grained Fe–14Cr and ODS Fe–14Cr model alloys, J. Nucl. Mater. 417 (2011) 213–216, https://doi.org/10.1016/j.jnucmat.2010.12.060.
[46] I. Hilger, X. Boulnat, J. Hoffmann, C. Testani, F. Bergner, Y. De Carlan, F. Ferraro, A. Ulbricht, Fabrication and characterization of oxide dispersion strengthened (ODS) 14Cr steels consolidated by means of hot isostatic pressing, hot extrusion and spark plasma sintering, J. Nucl. Mater. 472 (2015) 206–214, https://doi.org/10.1016/j.jnucmat.2015.09.036.
[47] X. Zhou, Y. Liu, L. Yu, Z. Ma, Q. Guo, Y. Huang, H. Li, Microstructure characteristic and mechanical property of transformable 9Cr-ODS steel fabricated by spark plasma sintering, Mater. Des. 132 (2017) 158–169, https://doi.org/10.1016/j.matdes.2017.06.063.
[48] M. Dadé, J. Malaplate, J. Garnier, F. De Geuser, F. Barcelo, P. Wident, A. Deschamps, Influence of microstructural parameters on the mechanical properties of oxide dispersion strengthened Fe-14Cr steels, Acta Mater. 127 (2017) 165–177, https://doi.org/10.1016/j.actamat.2017.01.026.
[49] A. Chauhan, F. Bergner, A. Etienne, J. Aktaa, Y. De Carlan, C. Heintze, Microstructure Characterization and Strengthening Mechanisms of Oxide Dispersion Strengthened (ODS) Fe-9 % Cr and Fe-14 % Cr Extruded Bars, vol. 495, 20176–19, https://doi.org/10.1016/j.jnucmat.2017.07.060.
[50] C.E. Lacy, M. Gensamer, The tensile properties of alloyed ferrites, Trans. Am. Soc. Met. 32 (1944) 88–110, https://doi.org/10.1016/j.molcatb.2003.10.012.
[51] M. Praud, F. Mompiou, J. Malaplate, D. Caillard, J. Garnier, A. Steckmeyer, B. Fournier, Study of the deformation mechanisms in a Fe-14% Cr ODS alloy, J. Nucl. Mater. 428 (2012) 90–97, https://doi.org/10.1016/j.jnucmat.2011.10.046.
[52] F. Bergner, C. Heintze, I. Hilger, M. Serrano, Elastic Properties of Fe-Cr and ODS Fe-Cr Alloys, 20161–2, https://doi.org/10.13140/RG.2.1.3783.5281.
[53] J.E. Bailey, P. Hirsch, The dislocation distribution, flow stress, and stored energy in cold-worked polycrystalline silver AU -, Philos. Mag. A J. Theor. Exp. Appl. Phys. 5 (1960) 485–497, https://doi.org/10.1080/14786436008238300.
[54] R.E. Stoller, S.J. Zinkle, On the relationship between uniaxial yield strength and resolved shear stress in polycrystalline materials, J. Nucl. Mater. 283–287 (2000) 349–352, https://doi.org/10.1016/S0022-3115(00)00378-0.
[55] A.K. Seeger, On the theory of radiation damage and radiation hardening, Proc. Second Unit. Nation Int. Conf. Peace Uses At. Energy 6 (6) (1958) 250–273, https://doi.org/10.1007/BF03223261.
[56] J.H. Kim, T.S. Byun, D.T. Hoelzer, C.H. Park, J.T. Yeom, J.K. Hong, Temperature dependence of strengthening mechanisms in the nanostructured ferritic alloy 14YWT: Part II—mechanistic models and predictions, Mater. Sci. Eng. A 559 (2013) 111–118, https://doi.org/10.1016/j.msea.2012.08.041.
[57] Z. Chen, Modeling the Plastic Deformation of Iron, 2012https://doi.org/10.5445/KSP/1000032216.
[58] F. Pickering, Structure-Property relationships in steels, Mater. Sci. Technol. (2006) https://doi.org/10.1002/9783527603978.mst0062.
[59] J. Isselin, R. Kasada, A. Kimura, T. Okuda, M. Inoue, S. Ukai, S. Ohnuki, T. Fujisawa, F. Abe, Evaluation of fracture behavior of recrystallized and aged high-Cr ODS ferritic steels, J. Nucl. Mater. 417 (2011) 185–188, https://doi.org/10.1016/j.jnucmat.2010.12.061.
[60] S. Mohan, G. Kaur, B.K. Panigrahi, C. David, G. Amarendra, Effect of Zr and Al addition on nanocluster formation in oxide dispersion strengthened steel - an ab initio study, J. Alloy. Comp. 767 (2018) 122–130, https://doi.org/10.1016/j.jallcom.2018.07.047.
[61] M.K. Dash, R. Mythili, R. Ravi, T. Sakthivel, A. Dasgupta, S. Saroja, S.R. Bakshi, Microstructure and mechanical properties of oxide dispersion strengthened 18Cr-ferritic steel consolidated by spark plasma sintering, Mater. Sci. Eng. A (2018) https://doi.org/10.1016/j.msea.2018.08.093.
[62] H. Dong, L. Yu, Y. Liu, C. Liu, H. Li, J. Wu, Enhancement of tensile properties due to microstructure optimization in ODS steels by zirconium addition, Fusion Eng. Des. (2017) https://doi.org/10.1016/J.FUSENGDES.2017.03.170.
[63] L. Zhang, L. Yu, Y. Liu, C. Liu, H. Li, J. Wu, Influence of Zr addition on the microstructures and mechanical properties of 14Cr ODS steels, Mater. Sci. Eng. A 695 (2017) 66–73, https://doi.org/10.1016/J.MSEA.2017.04.020.
[64] R. Rahmanifard, H. Farhangi, A.J. Novinrooz, Effect of zirconium and tantalum on the microstructural characteristics of 12YWT ODS steel nanocomposite, J. Alloy. Comp. 622 (2015) 948–952, https://doi.org/10.1016/j.jallcom.2014.11.018.